The role of process parameters and printing position on meltpool variations in LPBF Hastelloy X: Insights into laser-plume interaction

Author(s):
Tang, Jian; Wróbel, Rafał; Scheel, Pooriya; Gaechter, Willy; Leinenbach, Christian; Hosseini, Ehsan

Publication date:
2024-04

Permanent link:
https://doi.org/10.3929/ethz-b-000666203

Originally published in:
Additive Manufacturing Letters 9, https://doi.org/10.1016/j.addlet.2024.100203

Additive Manufacturing Letters 9 (2024) 100203

Contents lists available at ScienceDirect

Additive Manufacturing Letters

journal homepage: www.elsevier.com/locate/addlet

Short Communication

The role of process parameters and printing position on meltpool variations in LPBF Hastelloy X: Insights into laser-plume interaction

Jian Tang [a,b], Rafal Wróbel [a,c], Pooriya Scheel [a,b], Willy Gaechter [b], Christian Leinenbach [a,d], Ehsan Hosseini [a,*]

[a] Empa Swiss Federal Laboratories for Materials Science & Technology, 8600 Dübendorf, Switzerland
[b] Department of Mechanical and Process Engineering, ETH Zürich, 8092 Zürich, Switzerland
[c] Department of Materials, ETH Zürich, 8092 Zürich, Switzerland
[d] Laboratory for Photonic Materials and Characterization, École Polytechnique Fédérale de Lausanne, 1015 Lausanne, Switzerland

ARTICLE INFO

Keywords:
Laser powder bed fusion
Process parameter
Meltpool dimensions
Laser-plume interaction
Powder layer thickness

ABSTRACT

Meltpool dimensions play a pivotal role in defining the defects and microstructure state of Laser Powder Bed Fusion (LPBF) builds. Therefore, it is crucial to investigate variations in meltpool geometries under different process conditions. In this work, we fabricated single tracks of LPBF Hastelloy X (HX) alloy under 36 printing conditions and examined the corresponding cross-section meltpool dimensions at two locations across the build platform. This investigation demonstrates the impacts of laser power, scan speed, powder layer thickness, and printing locations on resultant meltpool dimensions. As expected, we observed that meltpool dimensions increase as laser power increases or scan speed decreases. It was also concluded that thicker powder layers lead to wider and shallower meltpools due to reduced laser energy penetration into the solid beneath the powder layer. Additionally, the meltpool dimensions show variations dependent on deposition locations due to the different levels of interaction of the laser and its induced vapor plume, resulting in shallower and wider meltpools. These findings provide a systematic understanding of meltpool dimension variations across various process conditions for LPBF HX alloy, which ultimately offer insights into the formation of defects and microstructure features.

1. Introduction

Additive manufacturing techniques, such as laser powder bed fusion (LPBF), have emerged as effective alternatives for producing metallic components with complex (internal) architectures. In LPBF, metal powder is deposited layer-by-layer, and a laser beam is used to selectively fuse sections of powder layers point by point based on a sliced CAD model [1]. This incremental and point-by-point manufacturing strategy enables the realization of metallic components with near-net shapes and even functionally graded properties [2].

Although LPBF has achieved significant success in fields such as aerospace, bio-implants, and more, it currently faces challenges in quality control. These are primarily due to a lack of understanding of the linkage between process, microstructure, and properties. Non-optimized process conditions can lead to defects such as pores and cracks, as well as inferior microstructures, which ultimately result in compromised end-use mechanical performance [3–5]. One critical feature governing defects and microstructure formation during the LPBF process is the meltpool size and shape [6,7]. For instance, a small or shallow meltpool (without sufficient hatching) can result in lack-of-fusion defects, while an overly large and deep meltpool may be accompanied by keyhole-induced defects [8–10]. Additionally, the geometry of the meltpool affects grain morphology and crystallographic texture [11]. Therefore, investigating the sensitivity of meltpool size and geometry to various process parameters is fundamental for understanding the linkage between process, microstructure, and properties in LPBF alloys.

In this work, we focus on a systematic study of Hastelloy X (HX) alloy, a solid-solution strengthened Ni-based alloy known for its exceptional high-temperature strength and hot corrosion resistance [12–14]. HX is commonly used in critical high-temperature components for applications such as gas turbines [15–17]. Numerous investigations have explored the characteristics of microstructure and the corresponding mechanical response in LPBF HX alloy [17–20]. For example, Ghiaasiaan et al. reported superior yield strength and enhanced ductility in LPBF HX alloy compared to its wrought counterparts, attributed to its finely deposited dendritic microstructure [19]. Esmaeilizadeh et al.

* Corresponding author.
E-mail address: ehsan.hosseini@empa.ch (E. Hosseini).

https://doi.org/10.1016/j.addlet.2024.100203
Received 20 December 2023; Received in revised form 21 February 2024; Accepted 26 February 2024
Available online 1 March 2024

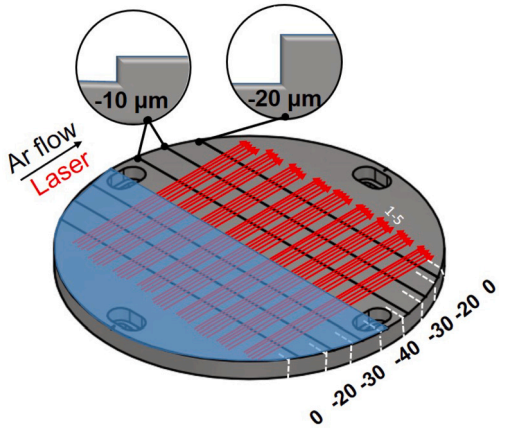

Fig. 1. A schematic of the customized substrate with the laser scanning tracks.

demonstrated that the ultimate tensile strength and ductility of LPBF HX decrease when the scan speed is either too low or too high due to the formation of lack-of-fusion or keyhole defects [18].

However, systematic investigations into how meltpool geometries change under various process conditions for LPBF HX alloy are still limited. This is despite their importance in understanding the formation of defects and microstructure, and consequently in quality control and advanced design for LPBF HX fabrications. To address this, Zhang et al. studied the effect of linear energy density (LED = P/v, the ratio of laser power to scan speed) on the meltpool size of single-track LPBF HX alloy, observing a larger meltpool under higher LED [21]. Similarly, Keshavarzkermani et al. investigated the influence of Laser LED and powder layer thickness on meltpool dimensions in HX alloy and reported a similar sensitivity of meltpool geometry to the LED [22]. However, their work did not reveal a clear trend in meltpool dimensions relative to changes in powder layer thickness, likely due to complications in analyzing data gathered from printing on top of the rough surfaces resulting from previous layer deposition. To provide a more comprehensive understanding of the sensitivity of meltpool geometry to the parameters of LPBF for HX alloy, we customized an HX substrate to allow the deposition of various layer thicknesses within a single recoating step over a smooth (machined) surface. The particular design of the substrate also enables the comparison of deposited material with the same set of process parameters at different locations within the build platform. By employing different sets of laser parameters on the designed substrate, we investigate the meltpool sensitivity to LPBF process conditions and printing positions by depositing single-track scans with 36 unique combinations of laser power, scan speed, and powder layer thickness.

2. Materials and methods

The customized printing substrate was manufactured from wrought HX through electro-discharge machining (EDM) and featured steps of varying depths (-20, -30, -40, -30, and -20 µm from left to right) in the middle of a 90 mm diameter round plate, as shown in Fig. 1. The width of the steps for depths of -20 and -30 µm was 7.5 mm, while that for the middle -40 µm step was 15 mm. These steps were then filled with powder, resulting in layer thicknesses of 20, 30, and 40 µm. Additionally, laser scanning at the two extreme sides of the substrate represents conditions without deposited powder layer, i.e. powder layer thickness of zero. The powder used in this study was gas-atomized HX powder supplied by Oerlikon AM with the composition, shape, and size distribution as reported in [17].

As summarized in Table 1, we studied nine sets of laser powers and scan speeds for the four powder layer thicknesses. For each combination, we deposited five 60 mm tracks on top of the substrate using a Sisma MySint 100 LPBF machine with a 200 W fiber laser under

Table 1
Examined process conditions for the single-track HX LPBF.

LED (J/mm)	Laser power *P* (W)	Scan speed *v* (mm/s)	Layer thickness *t* (µm)
0.223±0.003	200	900	
	175	800	
	125	550	
0.182±0.006	200	1100	
	175	900	0, 20, 30, 40
	125	700	
0.154±0.002	200	1300	
	175	1150	
	125	800	

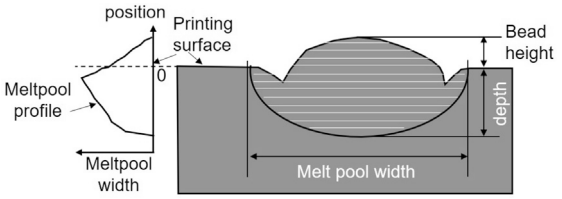

Fig. 2. A schematic illustrating the strategy for analyzing meltpool dimensions.

continuous-wave mode operation and Argon shielding gas. The flow direction of the shielding gas was the same as the laser scan direction. The laser spot had a diameter of 55 µm and a wavelength of 1070 nm. We used long dwell times of 2 minutes between tracks to minimize variations in meltpool dimensions due to heat accumulation in the substrate.

The meltpool dimensions for different conditions were assessed based on their cross-sections perpendicular to the scan direction at two different printing locations (i.e., left/beginning and right/end side of the substrate). Metallography sections were taken from the build (as indicated by the eight white dashed lines in Fig. 1) and polished to a 0.05 µm surface finish. They were then etched with Glyceregia reagent (HCl:HNO3:Glycerol = 3:1:2) for 2 minutes. The sections' locations were chosen to assess the steady-state dimensions of the meltpool later using scanning electron microscopy (SEM) (FEI Quanta 650).

We used an in-house MATLAB code to extract the meltpool dimensions from the SEM pictures. Width, depth, bead height, and "meltpool profile" were used for quantifying the meltpool geometry (See Fig. 2). The meltpool profile was defined as the width of the meltpool at different heights relative to the printing surface. This was calculated based on counting the horizontal pixels in the meltpool at different heights, excluding pixels of pores or voids in the meltpool area. We quantified the average, standard deviation, and confidence interval of meltpool features based on measurements from five tracks for each process condition.

3. Results and discussions

This section discusses the sensitivity of the meltpool geometry to various LPBF process parameters by evaluating meltpool depth, width, and bead height. Meltpool profiles and SEM images are also provided to interpret the observations where needed.

The supplementary materials report meltpool dimensions for all examined LPBF conditions. In the following discussions, for brevity, the focus on the sensitivity of meltpool geometry to laser power, scan speed, and printing position is based on observations from the conditions without deposited powder layer, as similar tendencies are observed for depositions with a powder layer. Section 3.3 then discusses the influence of powder layer thickness on meltpool dimensions and shape.

3.1. Effect of laser power and scan speed

Figs. 3a-d present the meltpool depth, width, bead height, and its depth-to-width ratio under various scan speeds and laser powers, re-

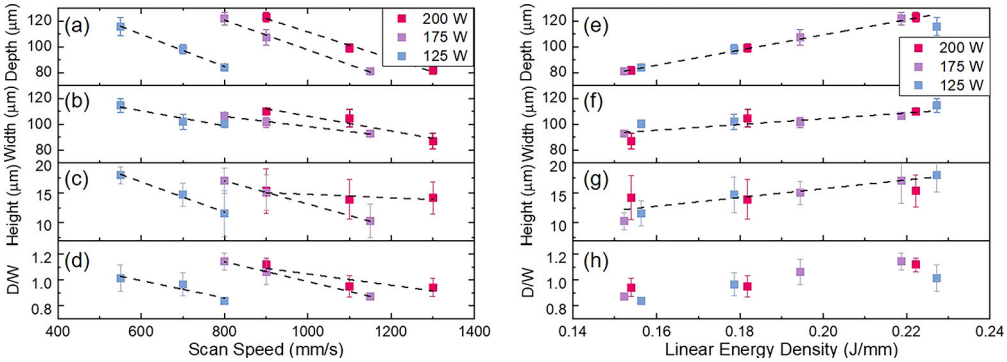

Fig. 3. Meltpool dimensions observed for single-track LPBF of HX alloy during the laser scan without deposited powder layer, as functions of (a-d) laser scan speed and power and (e-h) LED: (a, e) meltpool depth, (b, f) width, (c, g) bead height, and (d, h) depth-to-width ratio (D/W). Dashed lines indicate linear trends.

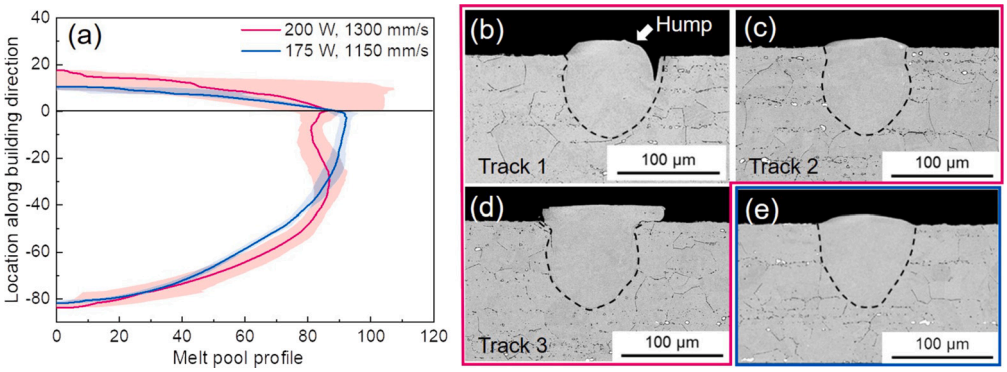

Fig. 4. (a) Meltpool profiles resulted from LED = 0.15 J/mm for the scan speeds of 1300 mm/s and 1150 mm/s; (b-d) corresponding SEM images depicting meltpool morphologies for scan speeds of 1300 mm/s and (e) 1150 mm/s. The shadow in (a) represents the 95% confidence interval of the meltpool profile.

spectively. The measured values are derived from SEM images taken from the beginning part of the tracks, i.e., located in the left half of the build plate and indicated by the blue area in Fig. 1. The sensitivity of the meltpool geometry to the printing position is discussed in the following section.

Meltpool depth, width, and bead height all decrease for higher scan speeds and lower laser powers. Fig. 3d shows a similar trend for depth-to-width ratio, which demonstrates the higher sensitivity of the meltpool depth to scan parameters. These results align well with previous reports [21,22], indicating a correlation between the amount of deposited energy in the laser path and meltpool dimensions. This correlation can be better observed in Figs. 3e-h, where the three dimensions consistently increase for higher linear energy density (LED) expressed as LED = P/V. LED efficiently combines the effects of laser power and scan speed on meltpool dimensions (especially for meltpool depth), similar to observations in [21,22].

Further insights into the sensitivity of meltpool shape to laser scan speeds can be inferred from comparing the SEM images and meltpool profiles. Fig. 4 compares the meltpool shapes for LED of approximately 0.15 J/mm and varying scan speeds of 1300 mm/s and 1150 mm/s. The meltpool formed under the lower scan speed exhibits a more regular shape with low variability among the different examined sections. In contrast, the meltpool formed under the fastest examined scan speed of 1300 mm/s is highly irregular, displaying significant variability and often featuring a hump. This irregularity can be attributed to rapid solidification under fast scan speeds, which provides insufficient time for molten metal surface tension to shape a regular-shape meltpool [23].

3.2. The effect of printing position

In the previous section, we discussed the effects of laser power and scan speed on the dimensions of the meltpool. In this section, we examine the differences in meltpool dimensions between the beginning and end parts of laser tracks. Our customized substrate and experimental design enabled an investigation into how sensitive meltpool dimensions are to the printing position under various LPBF process conditions.

Fig. 5 presents the dimensions of the meltpool formed during the laser scans with zero layer thickness for different sets of laser parameters at both the beginning and end of laser tracks. This indicates a sensitivity of meltpool sizes and shapes to the printing location across the build platform. At the lowest scan speed, the meltpool at the beginning of the tracks (solid points in Fig. 5) is shallower and slightly wider than at the track ends (half-opened points in Fig. 5). However, an opposite tendency is observed as the scan speed increases, where shallower and wider meltpools are observed at the end of the tracks. The difference in meltpool dimensions between these two printing positions becomes more significant for higher scan speeds and laser powers.

The observed dependence of meltpool geometry on the printing location and its sensitivity to laser parameters can be explained by considering the laser-plume effect. The plume refers to a hydrodynamics concept that describes the motion of a column or stream of fluid. In LPBF, this refers to the motion of vaporized metal and ionized plasma [24] and can cause absorption and scattering of the laser, leading to reduced effective laser intensity and a widened effective beam diameter. As a result, it often leads to the formation of a shallower and wider meltpool [25].

Interestingly, the plume intensifies under higher laser power, and its direction also changes depending on the scan speed [24,26]. The vapor plume usually ejects from the hottest spot in the meltpool, which experiences the most intensive metal vaporization [27]. Simulations in [28] have shown that the hottest location in the meltpool shifts from the rear to the bottom and then to the front side of the keyhole wall as the scan speed increases. Consequently, the ejection of the vapor plume changes accordingly from forward to backward. Meanwhile, the incident angle of the laser varies at different printing positions, as discussed in [29,30], despite the implementation of the F-theta lens in printing machines. The

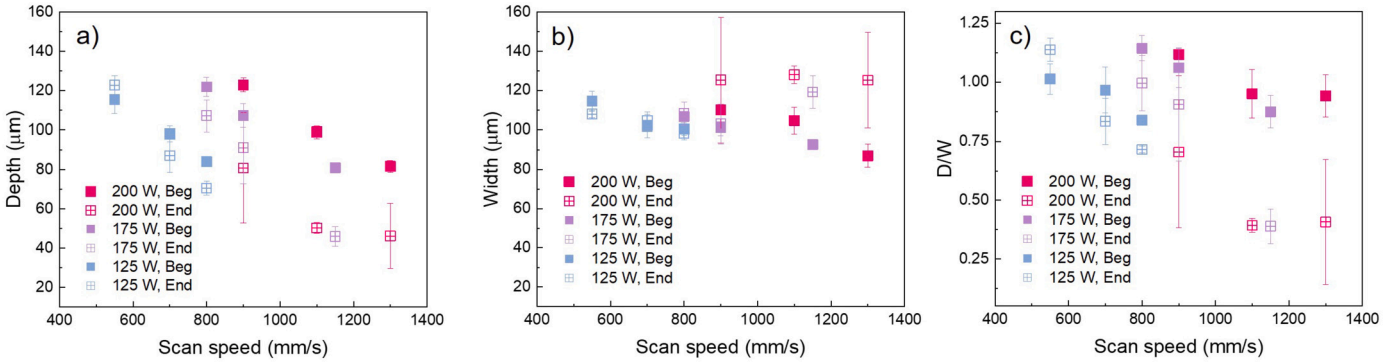

Fig. 5. Comparison of the meltpool dimensions formed during the laser scans without deposited powder layer on the left and right sides of the substrate, i.e. at the beginning and end of the laser tracks: (a) meltpool depth, (b) width and (c) depth-to-width ratio.

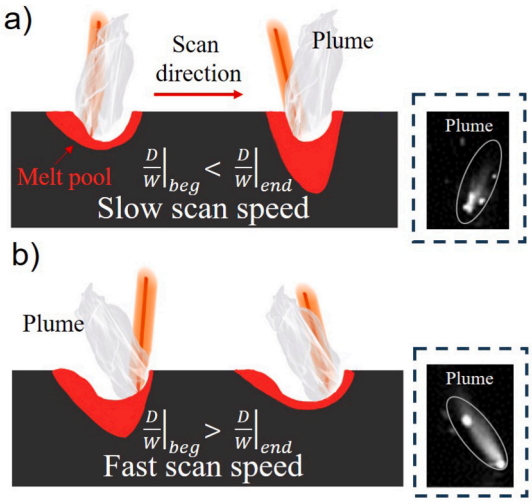

Fig. 6. Schematic of laser and plume interactions and their effects on the meltpool depth-to-width ratio under (a) slow and (b) fast scan speeds. The black, white, and red areas represent the solid, gas, and molten metal, respectively. Images in the dashed outline are high speed images of vapor plume under (a) slow and (b) fast scan speeds (Reproduced with permission from Ref. [26] Copyright 2018, Elsevier).

influence of the variation in laser beam inclination is evident in Fig. S1 of the Supplementary Materials, which shows that the centerlines of the meltpools at the corners of the build plate are tilted away from the vertical direction.

Accordingly, Fig. 6 shows a schematic of the laser-plume interaction under various laser scan speeds at different printing positions. At low scan speeds, the plume ejects forward and strongly interferes with the laser at the beginning of the tracks (blue area in Fig. 1), while it has only a marginal interaction at the end of the tracks (the gray area in Fig. 1). Therefore, a shallower and wider meltpool is expected at the beginning of the tracks under slow scan speeds (as the red area in Fig. 6a). On the other hand, at high scan speeds, the plume's direction shifts backward, resulting in a more pronounced laser-plume interaction at the end of the tracks compared to the beginning. This accounts for the reduced depth and increased width of the meltpool observed at the end of the track under fast scans (as the red area in Fig. 6b).

A non-uniform spatial distribution of inert gas flow velocity can also contribute to the position dependency of meltpool dimensions, as the gas flow can distort the vapor plume column and thus affect the intensity of interaction between the plume and the laser [31,32]. However, the evidence presented in this study suggests only a marginal effect from the inert gas flow. For most conditions (except with the lowest scan speed), a deeper meltpool is observed at the beginning of the tracks, i.e., closer to the inert gas inlet, contrary to what was expected if the inert gas had a dominant effect on the plume column distortion leading to a more intense interaction with the (inclined) incident laser beam. It should also be noted that observations of differences in meltpool dimensions under the same laser power and scan speed for different printing positions indicate that linear energy density (LED) cannot solely describe the dimensions of the meltpool, as it does not account for effects from, e.g., laser-plume interaction and its sensitivity to the deposition positions.

3.3. The effect of layer thickness

As meltpool dimensions at the beginning of the tracks are found to be less affected by the laser-plume interaction for most of the studied process conditions, we focused our analysis on the effect of powder layer thickness on the meltpool geometry at the initial part of the tracks (highlighted in blue in Fig. 1).

Fig. 7a and b show that as the powder layer thickness increases, the meltpool depth decreases while its width increases. This is attributed to laser absorption by the powder layer and the low thermal conductivity of the powder material, which results in reduced thermal energy penetration in the depth direction and more heat accumulation on the top of the meltpool, hence the formation of shallower and wider meltpools. Accordingly, there is a smaller depth-to-width (D/W) ratio for the meltpool as the powder layer thickness increases, as seen in Fig. 7c. The bead height in Fig. 7d generally increases with the powder layer thickness, except for the condition with the highest laser scan speed, where a large data variation is also observed, possibly due to the instability of the meltpool at high scan speeds [33].

The observations also reveal a significant increase in the variability of meltpool geometry when introducing the powder layer (see Fig. S2 in the supplementary materials). This heightened variability is likely attributed to the stochastic nature of powder layer characteristics and the interaction of the vapor jet with powder particles, leading to greater variability in the dimensions of the formed meltpool [34].

Fig. S3 in the supplementary materials displays meltpool dimensions at the end of the tracks for various layer thicknesses. A similar trend for the sensitivity of meltpool dimensions to layer thickness is observed there for most conditions, while a few inconsistencies under high scan speeds can be explained by the intensified laser-plume interaction at the end of the tracks.

4. Concluding remarks

In this work, single LPBF tracks were deposited under nine combinations of laser power and scan speed, and for four different layer thicknesses at two sides of a customized HX substrate (with five repetitions per condition). The cross-sectional meltpool geometries of the deposited single tracks were analyzed to evaluate their sensitivity to laser power, scan speed, powder layer thickness, and printing locations. The key findings include:

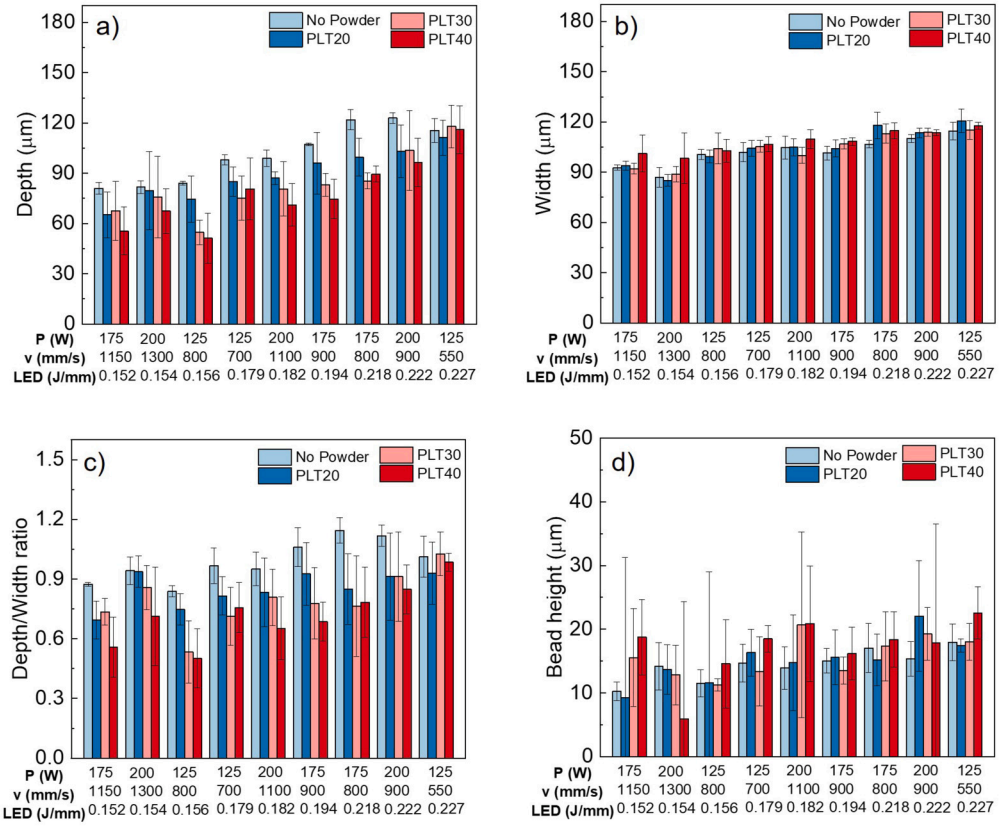

Fig. 7. Meltpool dimensions at the start of LPBF HX single-tracks with different powder layer thicknesses: (a) depth, (b) width, (c) depth-to-width ratio, and (d) bead height. The term "PLT" indicates powder layer thickness in micrometers (µm).

- The meltpool geometry varies at different printing locations, influenced by laser-plume interaction, which can cause an increase in effective laser beam diameters and reduced laser intensity, resulting in a wider and shallower meltpool. The evidence presented in this study suggests that variations in meltpool dimensions across positions are primarily due to differences in the laser's inclination angle at various locations and the sensitivity of the vapor plume to the laser scan speed and power. Additionally, it posits that the impact of non-uniform spatial distribution of inert gas flow velocity on meltpool dimension variations across the build platform is marginal.
- The meltpool depth and width increase with higher laser powers or slower scan speeds. However, the linear energy density parameter does not necessarily provide an accurate representation of meltpool dimensions, particularly in cases involving considerable laser-plume interaction.
- For a given set of laser parameters (and printing location), a shallower and wider meltpool with higher bead height is observed for the larger powder layer thicknesses.

It is important to acknowledge that the experimental method adopted in this study did not allow for the quantification of meltpool length, which could potentially provide deeper insights into the sensitivity of meltpool geometry to the LPBF process conditions. Therefore, future research that integrates in-situ imaging techniques, such as X-ray or high-speed thermal cameras, to observe meltpools and vapor plumes for single-track and multi-track multi-layer depositions could represent a pivotal direction for advancing understanding in this field.

CRediT authorship contribution statement

Jian Tang: Writing – original draft, Visualization, Validation, Resources, Methodology, Investigation, Formal analysis, Data curation. **Rafal Wróbel:** Writing – review & editing, Validation, Resources, Methodology, Investigation, Data curation. **Pooriya Scheel:** Writing – review & editing, Resources, Methodology, Investigation. **Willy Gaechter:** Writing – review & editing, Visualization, Validation, Resources, Formal analysis, Data curation. **Christian Leinenbach:** Writing – review & editing, Resources, Methodology, Conceptualization. **Ehsan Hosseini:** Writing – review & editing, Supervision, Project administration, Methodology, Funding acquisition, Conceptualization.

Declaration of competing interest

The authors declare that they have no known competing financial interests or personal relationships that could have appeared to influence the work reported in this paper.

Data availability

Data will be made available on request.

Acknowledgements

Financial support by the Swiss National Science Foundation (SNSF grant number 200551) is gratefully acknowledged.

Appendix A. Supplementary material

Supplementary material related to this article can be found online at https://doi.org/10.1016/j.addlet.2024.100203.

References

[1] ASTM ISO, ISO/ASTM 52900: 2015 additive manufacturing-general principles-terminology, ASTM F2792-10e1, vol. 1, 2015, pp. 1–19.

[2] K.A. Sofinowski, S. Raman, X.G. Wang, B. Gaskey, M. Seita, Layer-wise engineering of grain orientation (LEGO) in laser powder bed fusion of stainless steel 316L, Addit. Manuf. 38 (2021) 101809.
[3] E. Hosseini, V.A. Popovich, A review of mechanical properties of additively manufactured Inconel 718, Addit. Manuf. 30 (2019) 100877.
[4] T. DebRoy, T. Mukherjee, H.L. Wei, J.W. Elmer, J.O. Milewski, Metallurgy, mechanistic models and machine learning in metal printing, Nat. Rev. Mater. 6 (2021) 48–68.
[5] T. DebRoy, T. Mukherjee, J.O. Milewski, J.W. Elmer, B. Ribic, J.J. Blecher, W. Zhang, Scientific, technological and economic issues in metal printing and their solutions, Nat. Mater. 18 (2019) 1026–1032.
[6] J.B. Forien, N.P. Calta, P.J. DePond, G.M. Guss, T.T. Roehling, M.J. Matthews, Detecting keyhole pore defects and monitoring process signatures during laser powder bed fusion: a correlation between in-situ pyrometry and ex-situ X-ray radiography, Addit. Manuf. 35 (2020) 101336.
[7] S.I. Shahabad, U. Ali, Z.D. Zhang, A. Keshavarzkermani, R. Esmaeilizadeh, A. Bonakdar, E. Toyserkani, On the effect of thin-wall thickness on melt pool dimensions in laser powder bed fusion of Hastelloy X: numerical modeling and experimental validation, J. Manuf. Process. 75 (2022) 435–449.
[8] S.V. Adjamsky, Y.V. Tkachev, G.A. Kononenko, Effect of selective laser melting parameters on the melt pool formed by single tracks of the heat-resistant Inconel 718 nickel alloy, Powder Metall. Met. Ceram. 59 (9) (2021) 592–600.
[9] K.J. Dai, X. He, W. Zhang, D.C. Kong, R. Guo, M.L. Hu, K.T. He, C.F. Dong, Tailoring the microstructure and mechanical properties for Hastelloy X alloy by laser powder bed fusion via scanning strategy, Mater. Des. 235 (2023) 112386.
[10] K.J. Dai, X. He, D.C. Kong, C.F. Dong, Multi-physical field simulation to yield defect-free Inconel 718 alloy fabricated by laser powder bed fusion, Mater. Lett. 355 (2024) 135437.
[11] S. Hibino, T. Todo, T. Ishimoto, O. Gokcekaya, Y. Koizumi, K. Igashira, T. Nakano, Control of crystallographic texture and mechanical properties of Hastelloy X via laser powder bed fusion, Crystals 11 (9) (2021).
[12] H.U. Hong, I.S. Kim, B.G. Choi, H.W. Jeong, C.Y. Jo, Effects of temperature and strain range on fatigue cracking behavior in Hastelloy X, Mater. Lett. 62 (28) (2008) 4351–4353.
[13] X.Y. Wang, A. Dallemagne, Y.Q. Hou, S. Yang, Effect of thermomechanical processing on grain boundary character distribution of Hastelloy X alloy, Mater. Sci. Eng. A 669 (2016) 95–102.
[14] M. Aghaie-Khafri, N. Golarzi, Forming behavior and workability of Hastelloy X superalloy during hot deformation, Mater. Sci. Eng. A 486 (1–2) (2008) 641–647.
[15] H.E. McCoy, J.P. Strizak, J.F. King, Hastelloy X for high temperature gas-cooled reactor applications, Nucl. Technol. 66 (1) (1984) 161–174.
[16] J.C. Lippold, S.D. Kiser, J.N. DuPont, Welding Metallurgy and Weldability of Nickel-Base Alloys, John Wiley & Sons, 2011.
[17] J.U. Rakhmonov, C. Kenel, A. De Luca, C. Leinenbach, D.C. Dunand, Effect of Y_2O_3 dispersoids on microstructure and creep properties of Hastelloy X processed by laser powder bed fusion, Addit. Manuf. Lett. 3 (2022) 100069.
[18] R. Esmaeilizadeh, A. Keshavarzkermani, U. Ali, Y. Mahmoodkhani, B. Behravesh, H. Jahed, A. Bonakdar, E. Toyserkani, Customizing mechanical properties of additively manufactured Hastelloy X parts by adjusting laser scanning speed, J. Alloys Compd. 812 (2020) 152097.
[19] R. Ghiaasiaan, M. Muhammad, P.R. Gradl, S. Shao, N. Shamsaei, Superior tensile properties of Hastelloy X enabled by additive manufacturing, Mater. Res. Lett. 9 (7) (2021) 308–314.
[20] C.M. Pilgar, A.M. Fernandez, S. Lucarini, J. Segurado, Effect of printing direction and thickness on the mechanical behavior of SLM fabricated Hastelloy X, Int. J. Plast. 153 (2022) 103250.
[21] J. Zhang, X.W. Zong, Z. Chen, H.G. Fu, A numerical simulation and process optimization of a Hastelloy X alloy single track produced by selective laser melting, Trans. Indian Inst. Met. 75 (1) (2022) 101–111.
[22] A. Keshavarzkermani, E. Marzbanrad, R. Esmaeilizadeh, Y. Mahmoodkhani, U. Ali, P.D. Enrique, N.Y. Zhou, A. Bonakdar, E. Toyserkani, An investigation into the effect of process parameters on melt pool geometry, cell spacing, and grain refinement during laser powder bed fusion, Opt. Laser Technol. 116 (2019) 83–91.
[23] C. Tang, K.Q. Le, C.H. Wong, Physics of humping formation in laser powder bed fusion, Int. J. Heat Mass Transf. 149 (2020) 119172.
[24] P. Bidare, I. Bitharas, R.M. Ward, M.M. Attallah, A.J. Moore, Fluid and particle dynamics in laser powder bed fusion, Acta Mater. 142 (2018) 107–120.
[25] C. Tenbrock, T. Kelliger, N. Praetzsch, M. Ronge, L. Jauer, J.H. Schleifenbaum, Effect of laser-plume interaction on part quality in multi-scanner laser powder bed fusion, Addit. Manuf. 38 (2021) 101810.
[26] H. Zheng, H.X. Li, L.H. Lang, S.L. Gong, Y.L. Ge, Effects of scan speed on vapor plume behavior and spatter generation in laser powder bed fusion additive manufacturing, J. Manuf. Process. 36 (2018) 60–67.
[27] H. Chen, W.T. Yan, Spattering and denudation in laser powder bed fusion process: multiphase flow modelling, Acta Mater. 196 (2020) 154–167.
[28] S.M.H. Hojjatzadeh, N.D. Parab, W.T. Yan, Q.L. Guo, L.H. Xiong, C. Zhao, M.L. Qu, L.I. Escano, X.H. Xiao, K. Fezzaa, et al., Pore elimination mechanisms during 3D printing of metals, Nat. Commun. 10 (1) (2019) 3088.
[29] P. Fathi-Hafshejani, A. Soltani-Tehrani, N. Shamsaei, M. Mahjouri-Samani, Laser incidence angle influence on energy density variations, surface roughness, and porosity of additively manufactured parts, Addit. Manuf. 50 (2022) 102572.
[30] S. Sendino, S. Martinez, A. Lamikiz, F. Lartategui, M. Gardon, J.J. Gonzalez, Analytical study of the melt pool distortion in the laser powder bed fusion process caused by the angle of incidence of the laser and its effect on the surface finish of the part, IOP Conf. Ser., Mater. Sci. Eng. 1193 (2021) 012010, IOP Publishing.
[31] J. Reijonen, A. Revuelta, T. Riipinen, K. Ruusuvuori, P. Puukko, On the effect of shielding gas flow on porosity and melt pool geometry in laser powder bed fusion additive manufacturing, Addit. Manuf. 32 (2020) 101030.
[32] D.A. Griggs, J.S. Gibbs, S.P. Baker, R.W. Penny, M.C. Feldmann, A.J. Hart, A testbed for investigation of laser powder bed fusion at elevated atmospheric pressure, Addit. Manuf. 51 (2022) 102581.
[33] I. Yadroitsev, I. Yadroitsava, A step-by-step guide to the LPBF process, in: Fundamentals of Laser Powder Bed Fusion of Metals, Elsevier, 2021, pp. 39–77.
[34] Q.L. Guo, C. Zhao, L.I. Escano, Z. Young, L.H. Xiong, K. Fezzaa, W. Everhart, B. Brown, T. Sun, L.Y. Chen, Transient dynamics of powder spattering in laser powder bed fusion additive manufacturing process revealed by in-situ high-speed high-energy X-ray imaging, Acta Mater. 151 (2018) 169–180.